

Design and field-of-view calibration of 114–660 GHz optics of the Earth Observing System Microwave Limb Sounder

Richard E. Cofield, *Member, IEEE*, and Paul C. Stek

Abstract—This paper describes the optics design and field-of-view (FOV) calibration for 5 radiometers covering 114 to 660 GHz which share a common antenna in the Microwave Limb Sounder instrument on NASA's Aura satellite. Details of near field pattern measurements are presented. Estimated systematic scaling uncertainties (3σ) on calibrated limb emissions, due to FOV calibration uncertainties, are below 0.4%. 3σ uncertainties in beamwidth and relative pointing of radiometer boresights are 0.006° and 0.003° , respectively. The uncertainty in modeled instrument response, due to the scan dependence of FOV patterns, is less than ± 0.24 K equivalent black-body temperature. Refinements to the calibration using in-flight data are presented.

Index Terms—remote sensing, calibration, near field range, microwave optics.

I. INTRODUCTION

THE Earth Observing System (EOS) Microwave Limb Sounder (MLS) instrument [1], [2] was launched aboard the Aura spacecraft on 15 July 2004. EOS MLS measures thermal microwave emission from the Earth's limb in order to determine composition and temperature of the atmosphere at altitudes between ~ 8 km and ~ 90 km.

Aura flies in a circular 705 km, 98° inclination, sun synchronous orbit with a 1:45 pm ascending node time. The MLS antennas vertically scan the limb approximately 3000 km in front of the spacecraft every 24.7 seconds, observing tangent heights between 8 and 90 km. The scan rate and the orbital speed are such that the tangent points during a scan are all approximately over the same point on the Earth's surface. The algorithm for positioning the antenna takes into account the spacecraft attitude and the Earth's oblateness, however the pointing requirement is far looser than the requirement for the knowledge of that pointing.

EOS MLS has 3 main elements, or modules: 1) the *GHz module* consists of an antenna and components that calibrate and down-convert portions of the received 114 to 660 GHz spectrum to bands up to 1.5 GHz wide centered near 900 MHz. 2) The *THz module* has the same purpose for bands near 2.5 THz. 3) The *Spectrometer module* contains 31 spectrometers which analyze the outputs of the GHz and THz modules

with resolution from 0.1 to 500 MHz. Measurement bands in the GHz module are grouped by shared local oscillators into 5 heterodyne radiometers: 2 centered near 118 GHz (R1A and R1B) plus 3 others at 190 GHz (R2), 240 GHz (R3) and 640 GHz (R4), and their optical paths out to a $1.6\text{ m} \times 0.8\text{ m}$ diffraction-limited primary aperture. The critical pressure and temperature measurements at 118 GHz have redundancy by observing both polarizations; R1A measures emission polarized vertically (electric field parallel to the nadir vector at the limb tangent point, altitude h_T) and R1B is polarized horizontally.

The final data products from MLS are defined on surfaces of constant pressure, not altitude. In addition, the retrieval algorithm is far more sensitive to the relative pointing of the various frequency bands in the instrument than to the absolute value of the pointing relative to the Earth. For these reasons, the boresight pointing of radiometers in both GHz and THz modules is primarily defined relative to the boresight at 234 GHz, which corresponds to a spectral line of $O^{18}O$ that is particularly well suited for measuring atmospheric pressure.

The raw data from MLS are transferred to the ground where they undergo several levels of processing: Level 1 takes the raw uncalibrated data, referred to as Level 0, and applies calibration factors to give the measured spectral brightness [3], or *radiance*, for each spectrometer channel. Each MLS radiance is proportional to received power, but for convenience it is expressed in intuitive units of Kelvins (K), so that in the long wave (Rayleigh-Jeans) limit the measure converges to the absolute temperature, T , of a black body emitting that amount of power. Level 2 uses a forward model to generate the radiance expected from an assumed atmosphere for the field of view and frequency of each channel for several vertical scans. This is compared to the actual measurements and iterated to produce local atmospheric quantities, such as composition and temperature, that yield calculated radiances which fit the observations.

The field of view (FOV) of the MLS instrument is defined [1] as its response to incident radiation as a function of angle. This paper describes the GHz optics design, alignment and performance, and calibration of its FOV on a near-field range. FOV calibration of the THz module is described in [4]. The co-alignment between GHz and THz FOVs is discussed here.

II. REQUIREMENTS AND DESIGN

FOV requirements given in [5] and repeated in Table I fall in two categories: 1) performance requirements on Half

Manuscript received May, 2005; revised October, 2005. The research described in this paper was carried out at the Jet Propulsion Laboratory, California Institute of Technology, under a contract with the National Aeronautics and Space Administration.

The authors are with the Jet Propulsion Laboratory, California Institute of Technology, Pasadena, CA 91109-8099. R. Cofield may be contacted at 818-354-2501 or Richard.E.Cofield@jpl.nasa.gov.

Power Beam Width (HPBW), beam efficiency, pointing and FOV scan; and 2) a FOV calibration requirement which limits the allowable errors induced by imperfect knowledge of the FOV shape. In practice, we establish compliance with both sets of requirements from measurements of the FOV in the ground environment, augmented with analytical models when the space environments (thermal, dynamic, *etc.*) cannot be simulated before launch or for FOV regions that are impractical to measure (*e.g.* far sidelobes). For calibration we divide the 4π solid angle domain of the FOV in two parts, conforming to Levels 2 and 1 of MLS data processing: The first part is Ω_A , the cone extending $\sim \pm 6^\circ$ about the nominal boresight direction. We provide the antenna directivity $G_b^A(\theta, \phi)$ inside Ω_A to the MLS forward model [6] to produce coefficients used in Level 2 processing to retrieve geophysical parameters. In Ω_A both atmospheric signal and the FOV vary rapidly with angle. Subscript b denotes the band frequency dependence of the FOV functions supplied; an error summary below shows that an even weaker scan angle dependence has little effect in the forward model. For the second part, we integrate far sidelobes over the remaining $4\pi - \Omega_A$. These antenna transmissions have negligible frequency dependence within each radiometer and negligible scan dependence overall. We provide them, along with antenna ohmic loss terms, to both the forward model and Level 1 for calibration of radiances [7].

In designing the antenna, a reflector system was the only candidate considered capable of meeting the FOV calibration requirement with an electrically large aperture ($D \sim 3500\lambda$ at 660 GHz) over a scan range approaching $100 \times \text{HPBW}$. The EOS MLS dual offset reflector design avoids blockage, and produces both a compact antenna and a moderately large f/D for demultiplexing the radiometer bands quasi-optically. A flat tertiary reflector folds the signal beam along a scan axis into a box housing calibration optics, an optical demultiplexer, and the radiometers. The antenna can be scanned over a 12° range (2° covering the atmosphere plus allowance for Earth oblateness and special operations) using a scan actuator mechanism attached between the antenna and the GHz module structure. A high-precision encoder on the scan axis reports the scan angle at 12 Hz synchronous with the radiometer data for ground processing.

At the input to the optical demultiplexer is a 45° switching mirror that rotates about an axis co-aligned with the incoming optical path. This mirror directs the radiometers' views to the antenna, cold space, or one of two warm targets. Consequently, the calibration path does not include the antenna, so the ohmic losses and emission from the three antenna reflectors must be inferred from ground calibration and temperatures measured by sensors mounted to the antenna elements.

A. Antenna

The antenna system for the GHz module has the same offset Cassegrain prescription as did its predecessor, the Upper Atmospheric Research Satellite (UARS) MLS [8], with properties shown in Figure 1. The surface figure and roughness requirements, derived from Ruze scattering theory [9], are tighter than those for UARS MLS to accommodate higher frequency radiometers (240 and 640 GHz). Based on experience

TABLE I
FOV REQUIREMENTS AND DESIGN SPECIFICATIONS.

	R1A	R1B	R2	R3	R4
HPBW / °					
Vertical	≤ 0.123	≤ 0.123	≤ 0.085	≤ 0.066	≤ 0.028
Horizontal	≤ 0.283	≤ 0.283	≤ 0.189	≤ 0.189	≤ 0.189
Beam Efficiency	≥0.95				
Boresight coincidence relative to R3 reference / °					
Vertical	≤0.025				
Horizontal	≤0.05				
FOV scan plane	within 1° of orbit plane				
FOV Boresight direction					
placement	[±0.01, ±0.02]° over 1 limb scan (25 s)				
angle knowledge	2 arcsecond (3σ) over time scale [0.17, 25] s				
rate knowledge	1 arcsecond (3σ) over time scale [0.17, 25] s				
jitter	2 arcsecond (3σ) over time scale < 0.17 s				
FOV Calibration: radiance errors induced by FOV knowledge uncertainties.					
absolute	≤3 Kelvin				
spectrally varying	≤1% or 0.03 Kelvin				
Nominal Edge Taper / dB					
Primary Reflector	-20	-20	-30	-30	-44
elsewhere	-40	-20	-40	-40	-50

from UARS MLS [10], where frequency dependent spillovers complicated the radiometric calibration, optics on EOS MLS are under-illuminated as shown in Table I. The edge truncation for R4 was made particularly low to allow for the expected greater surface inaccuracy near the edge of the antenna.

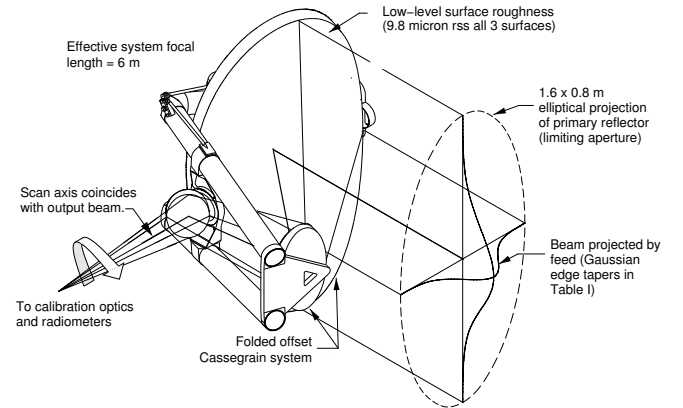


Fig. 1. EOS MLS GHz module antenna concept, showing Cassegrain configuration, edge tapers and surface tolerances of the reflectors.

The EOS MLS antenna, unlike the one on UARS MLS, is exposed to direct sunlight during a portion of each orbit, due to its location at the front of Aura and its along-track FOV. An all-aluminum construction antenna like the one used on UARS MLS would deform in response to orbital variation in solar illumination such that HPBW could vary by 25%. This would cause a measurement artifact that would be difficult to remove. To minimize thermal distortion, the primary is a lightweight egg-crate structure joining two skins and is constructed solely of low thermal expansion graphite epoxy. The front surface is bead-blasted for thermal radiative properties, then coated with

vacuum-deposited aluminum for high microwave reflectivity and to avoid reflecting sunlight, followed by silicon oxide for high infrared emissivity. The secondary and tertiary reflectors are solid aluminum with diamond-turned reflective surfaces and lightweight truss structures machined on the back. Their front surfaces were then grit-blasted to obtain the desired radiative properties. They are positioned relative to the primary and radiometer chassis on a composite cradle to preserve alignment over temperature and under dynamic loads, while scanning the collimated FOV through Earth's limb.

B. Optical Multiplexer

As for UARS MLS, the incoming signal was split among the GHz radiometers using a multiplexer consisting of a wire grid polarizer and three dichroic plates. Thicknesses, hole patterns, and hole shapes (circular, oval, and rectangular) varied between the dichroic plates to meet bandwidth and insertion loss requirements [11]. The feed mirrors coupling the antenna beam into corrugated horns on the GHz mixers had toric conic prescriptions, like those of UARS MLS, to match the astigmatic beam coming from the 2:1 aspect ratio antenna to the axisymmetric horn patterns. Throughout the multiplexer, surfaces at grazing incidence were kept outside the -75 dB contour of the nominal Gaussian beam, and aperture edge tapers outside contours in Table I. Figure 2 shows a schematic diagram, followed by the layout of beam splitters, radiometers, support structure, and signal beam paths, viewed from the unshaded side of the radiometer chassis with the antenna and covers removed.

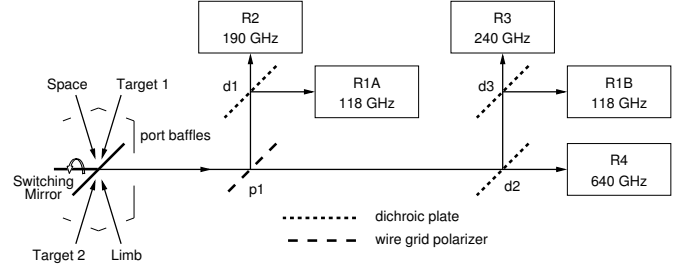
C. Analytical Model Repertory

We used the optical analysis tools which we had developed for UARS MLS [8], to design the EOS MLS optics and to establish its alignment tolerances. These models included: Fraunhofer diffraction and Geometrical Theory of Diffraction between Earth's limb and the GHz aperture, Geometrical Optics between primary and secondary reflectors, and Gaussian Beam Optics from the secondary reflector to the feed horn apertures. In addition, we applied models, based on Physical Optics, which are now easier to use, more widely available and faster than at the time of UARS MLS development. These tools let us verify component measurements, and substitute analysis for certain measurements that are too difficult or expensive with a large flight instrument.

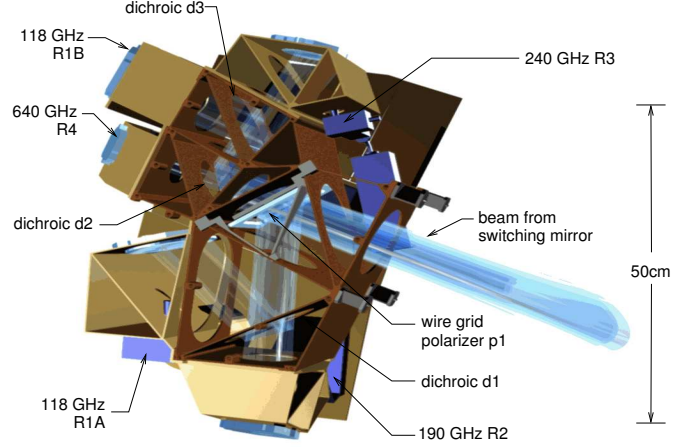
D. Tolerance methodology

Having verified the design with the Gaussian beam propagation module of a ray-trace program, we determined tolerances by calculating the overlap integral between two Gaussian beams: one from the nominal feed, and another produced by the optics between feed and antenna, perturbed by misalignments. Evaluating that integral gives the fractional intensity coupling between nominal and misaligned beams:

$$\mathcal{I}/\mathcal{I}_0 = \frac{w_{0x}w_{0y}}{w_xw_y} \times \frac{A_{0x}A_{0y}}{|A_x||A_y|} \exp(-C_x - C_y) \times \left| \exp\left(\frac{B_x^2}{A_x}\right) \right| \left| \exp\left(\frac{B_y^2}{A_y}\right) \right| \quad (1)$$



(a) schematic showing topology of switching mirror, ports, beam splitters and radiometers.



(b) layout, without switching mirror, targets and ports.

Fig. 2. GHz module optical multiplexer and radiometers.

$$\text{where } A_p = \left[\frac{1}{w_{0p}^2} + \frac{1}{w_p^2} \right] + \frac{j\pi}{\lambda R_p}$$

$$A_{0p} = 2/w_{0p}^2$$

$$B_p = j\pi\theta_p/\lambda$$

$$C_p = (\Delta_p/w_p)^2$$

$$w = \text{Gaussian beam radius at } 1/e \text{ intensity}$$

for $p = x$ and y . Subscript 0 denotes the nominal beam, and the perturbed beam has parameters

$$\theta_p = \text{tilt angles,}$$

$$\Delta_p = \text{decenters, and}$$

$$R_p = \text{phase radii.}$$

$\mathcal{I}/\mathcal{I}_0$ is the *Strehl ratio*, from which we supplied an rms wavefront error for the tolerancing algorithm of the program, thereby generating alignment sensitivities for small rigid-body motions of all optical elements. We inverted and adjusted these, based on manufacturing capabilities, to develop fabrication and assembly tolerances for the optical system.

Performance of the optics under orbital heat loads was predicted with a structural model that calculated deformations due to expected temperature fields. In turn, these were input to an optics model that calculated FOV performance. We also modeled dimensional changes of the composite components due to dehydration after launch, dynamic loads expected for launch and during operation, and gravitational loads expected in the FOV calibration configuration. We combined these

results with the fabrication tolerance budget, to partition tolerances between pre- and post-FOV calibration activities and to specify the number of measurements required for calibration.

III. ASSEMBLY, PERFORMANCE VERIFICATION, AND FOV CALIBRATION

A. Alignment

Components of the GHz module generally do not have surfaces that are specular under visible light: antenna reflectors have surfaces roughened for thermal radiative properties, and the grid and dichroic elements are periodic surfaces with spacings far greater than a wavelength of visible light. Hence they must be aligned using mechanical features, or displaced optical fiducial surfaces, related by coordinate transformations. Exceptions are the planar switching mirror and the toric feed mirrors, all with diamond-turned surfaces, which are inside the chassis, sheltered from the Sun. Since the feed mirrors distort visible light images, and access to alignment surfaces on the mixer feed horns is limited, we added small fiducial surfaces on the sides of feed mirrors for reference in the receiver alignment described below.

The tolerance budget identified receiver alignment as the most critical component of overall performance, so receivers were aligned using coherent radio frequency (RF) sources, rather than mechanical or optical techniques. End-to-end alignment was verified in FOV calibration performed on the near-field range described below. A final alignment of the GHz and THz boresight directions to the Aura master coordinate system was planned as a contingency, using shims in the installation of modules onto the spacecraft. However, during final module tests and spacecraft integration, alignment cube measurements showed that the alignment of boresights to mounting interfaces (and between interfaces) was within design allocations, so no shimming was required.

1) *Antenna Alignment:* The surface figure of each antenna reflector was evaluated throughout its fabrication by fitting appropriate conic surfaces to coordinate measuring machine (CMM) data. The shape of each best-fit surface is described by either 1 or 2 conic constants, plus 5 rigid-body misalignments, expressed in a coordinate system fixed to an alignment prism mounted on the back of each reflector. Antenna assembly included theodolite surveys of all these prisms. This verified that reflector shims, pre-computed from the best-fit surfaces, aligned the reflectors correctly, and defined the output (scan) axis of the antenna. Tooling balls, at locations also measured in these systems, permitted us to monitor the alignment through assembly and test of the GHz module using mechanical metering rods rather than optical equipment. The scan axis and scan bearings were aligned to the radiometer chassis at the limb port interface using optical tooling.

2) *Switching Mirror Alignment:* The switching mirror was aligned to the limb port and to the 640 GHz radiometer's interface plane using reticle mirrors in tooling matched to each interface datum. At this time the switching angles corresponding to limb and space views were established using alignment telescopes at the two port interfaces.

Alignment of the optical multiplexer was based on CMM data around the clear apertures of beam splitters, combined

with measurements of the multiplexer structure. This alignment was verified by insertion loss measurements and by near-field range patterns, both described below

3) *Receiver Alignment:* The GHz receiver front ends (RFEs), including feed mirrors and horns, were aligned during final subsystem assembly in an anechoic chamber built to accommodate far field feed pattern measurements. Both amplitude and phase patterns are required to completely describe the illumination of the antenna by its feed; we measured these feed patterns at the same frequencies planned for the subsequent near-field range tests, using electronics developed for that range. Feed patterns were referred to mechanical and optical features on the receiver using alignment telescopes and theodolites. To set up the range, an alignment telescope was registered to coordinates formed by axes of roll, azimuth and elevation positioners and two translation stages.

Radiation patterns of the feed horn had been measured relative to gage blocks bonded to the mixer body. Before delivery to the range, the feed mirror, horn/mixer assembly and feed mirror structure were assembled with nominal shims. The co-alignment of the the optical bench mounting interface, mirror, gage block and horn body was verified in a CMM survey capturing all mechanical features. Next, the RFE was installed on positioners and aligned to the telescope, except in axial position. Using a theodolite, we transferred alignment from the telescope to the transmitter (which now obscured the telescope).

After establishing co- and cross-polarized angles for transmitter and RFE, we measured principal plane patterns at several intermediate frequencies (IFs), obtaining pointing angles, lateral and axial phase centers and beamwidths. To control these 8 quantities we had 6 degrees of freedom available (2 tilts and 1 defocus at each of 2 interfaces: mixer horn to structure and feed mirror to structure). However, we used only the three mirror shims to adjust pointing angles and the mean axial phase center; changes in the other quantities (lateral phase center, beamwaist separation and beamwidth) were acceptably small. A second round of patterns confirmed the desired change in patterns, or led to a revised set of shims; after 4 iterations learning with the first RFE, we needed only 1 or 2 iterations to align subsequent units.

At this point another CMM dataset verified the desired shimming and established a baseline before environmental (thermal and vibration) tests of the RFE. After these tests, we took a third CMM dataset and measured principal plane patterns to verify negligible change due to vibration.

B. Feed Patterns

After each RFE was aligned, its FOV was characterized by amplitude and phase patterns in both co- and cross-polarization, out to 20° from boresight. Pattern cut spacing of 22.5° ensured that sampling of the 2:1 beam aspect ratio would be adequate for a subsequent spherical wave expansion (SWE) of the feed pattern about a nominal location of the receiver. A complete set of patterns was measured at each of about 7 frequencies chosen in both sidebands (except for the single sideband receivers R1A and R1B) to cover the expected

IF dependence of feed patterns, and to provide a baseline for comparison with aperture distributions measured later on the near-field range.

The SWE allows accurate reconstruction of the fields at near and intermediate distances from the receiver, such as at

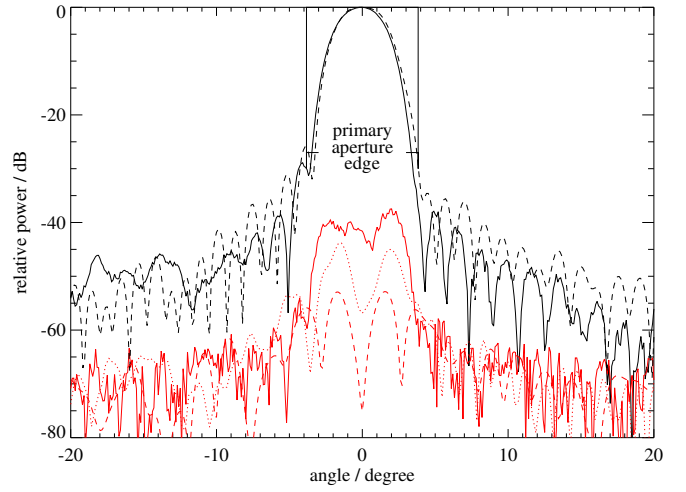
- 1) planar elements of the optical multiplexer, and
- 2) the baffles in the switching mirror cavity, which are limiting apertures for the limb, space, and target views of radiometric calibration.

For example, Figure 3 shows principal plane amplitude cuts at one frequency of the R3 radiometer. For this frequency a set of principal plane feedhorn patterns (co-polarized amplitude and phase) had been measured in horn acceptance testing. Given the nominal circular symmetry of the horn, these two cuts sufficed to generate a complete SWE of the fields which would illuminate the feed mirror. The figure compares the patterns calculated from Physical Optics scattering of these fields, by a nominally aligned feed mirror, with the measured receiver patterns. We attribute differences between these patterns to small asymmetries of the corrugated horn, and to the shim adjustment at the feed mirror mounts which aligned the receiver beam to its mechanical interface with the optical multiplexer.

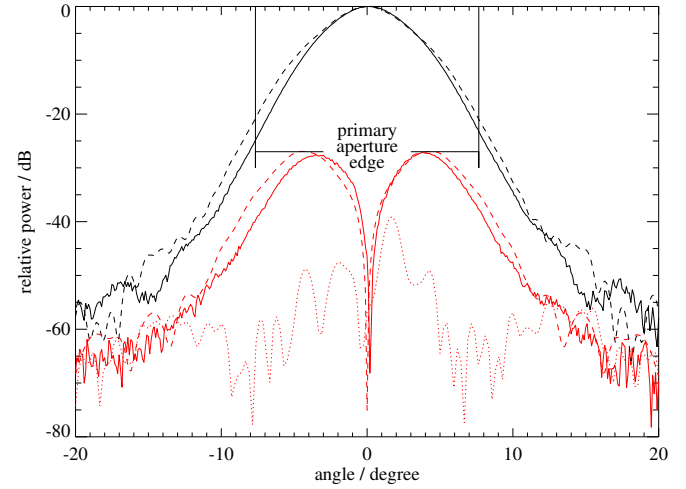
A fifth curve in each panel of Figure 3 shows the cross-polarized amplitude we expect after the beam passes through the wire grid polarizer $p1$. The calculation begins with a SWE of the measured RFE patterns. From this we evaluate fields incident on the grid, whose center is located $0.2z_{Rx}$ and $1.7z_{Ry}$ from the principal waists of the nominal feed beam having Rayleigh lengths z_{Rx}, z_{Ry} , *i.e.* in the near field. Finally we assume ideal behavior of the grid to calculate surface currents and superpose their radiated fields with the incident fields. The resulting far-field patterns are largely unchanged in the co-polarized component, but reduced in cross-polarization, especially on the optical axis, which explains the low values found in near field data. That is, feed pattern cross-polarization, caused by both the curvature and f/D of the offset feed mirror (shown here) and by non-idealities of the dichroic plates, is suppressed by having the polarizer as the multiplexer element nearest to the switching mirror. The suppression increases for the grid in the far field of the feed beam, hence is least for R1 and greatest for R4.

C. Baffle and Antenna Transmissions

Feed patterns were integrated out to the projected outlines of the limb, space, and target ports, and to edges of the antenna reflectors. These provide optical transmissions for radiometric calibration and for estimating radiance offsets, respectively, in the Level 1 radiance calibration algorithm. Values were interpolated from the measurement frequencies to signal and image sideband centers and provided to data processing software. Edge illumination levels were also used to calculate losses due to edge diffraction and surface scattering (using the Ruze theory); details are in [12]. Table II summarizes these optical losses averaged over all bands in each radiometer.



(a) E-plane



(b) H-plane

Fig. 3. 242.64 GHz feed patterns, co-polarized (black) and cross-polarized (red): Solid lines show patterns measured during receiver alignment, while dashed lines are predictions from measured feed horn patterns using Physical Optics. Dotted lines (cross-polarized only) result from propagating measured patterns through the wire grid polarizer $p1$ using the Physical Optics model, to explain the low cross-polarization levels seen later in the antenna aperture (within edges whose projection into feed angles is also shown here).

D. Ohmic Loss

Ohmic loss is a significant factor in radiometric calibration for the EOS MLS GHz module [7]. The loss is greater than for UARS MLS, since the smaller wavelengths of EOS MLS approach the scale of reflector surface roughness, and since EOS MLS reflector temperatures vary more in the polar orbit.

We inferred ohmic loss of the antenna reflectors from reflectivity measurements in several bands in all GHz radiometers (except R1B), using a radiometric insertion loss technique. The configuration uses the GHz space view in the same way as for linearity and sideband calibration, described in [7]. The RFE FOVs were switched between an external target, cooled in a liquid nitrogen bath and viewed by reflection at

TABLE II
REFLECTIVITIES, DIFFRACTION/SPILLOVER LOSSES, AND BAFFLE
TRANSMISSIONS OF THE GHz ANTENNA AND RADIOMETERS

	R1A	R1B	R2	R3	R4
Reflectivity = 1 - ohmic loss (after in-orbit adjustment)					
ρ_r^1	0.9977	0.9941	0.9968	0.9926	0.9889
ρ_r^2	0.9977	0.9939	0.9969	0.9924	0.9963
ρ_r^3	0.9984	0.9914	0.9978	0.9893	0.9949
$\prod_{k=1}^3 \rho_r^k$	0.9938	0.9795	0.9914	0.9746	0.9802
scattering and edge diffraction					
η_r^{AS}	0.9997		0.9993	0.9988	0.9916
η_r^{AD}	0.9990	0.9967	0.99986	0.99986	0.99997
η_r^{AA}	0.9987	0.9964	0.9992	0.9987	0.9916
primary spillover					
$\eta_{i,s}^1$	0.9812	0.9787	0.9952	0.9966	0.9972
$\eta_r^{AA} \eta_{i,s}^1$	0.9800	0.9753	0.9945	0.9953	0.9888
η_r^{MX} port baffle transmissions					
$X = L$ Limb	0.99598	0.99344	0.99901	0.99929	0.99907
$X = S$ Space	0.99587	0.99317	0.99903	0.99928	0.99907
$X = T$ Target	0.99575	0.99274	0.99902	0.99929	0.99907

45° incidence, and an adjacent ambient target. Two witness specimens, delivered with the primary reflector, had undergone the same thermal cycling and bead-blasting as the reflector. No such samples were made with the other reflectors, hence for the pre-launch calculation we substituted the primary's reflectivity, corrected for incidence angle at the secondary and tertiary using the Fresnel plane wave reflection formulæ [3, §4-12].

Reflectivity was found to decrease with frequency, as expected for the loss mechanism being surface micro-structure. Using calculated reflectivities of the silver plate standard, the measured reflectivity ranged from $\rho_{R1A}^1 = 0.9983$ to a worst-case value of $\rho_{R4}^1 = 0.9839$ with standard deviation of 0.0007. Values in Table II have been adjusted using in-orbit data as described below.

E. Radiometric verifications of optics performance

We measured transmission and reflection losses of the multiplexer optical elements by exchanging surrogate elements (solid plates and empty apertures) for the splitters while the assembled flight model radiometers viewed hot and cold targets alternately. Measured losses ranged from 0.01 dB (near the measurement threshold) to 0.3 dB, and met all requirements by factors of at least 2.

In two more radiometric tests, also performed during integration of the GHz module, we filled the switching mirror and antenna views with loads having large thermal contrast (100–200 K). These confirmed that optical transmissions had the high values claimed from feed pattern integration. Detailed results of these tests are discussed in [7].

The first, called the “dual cold load” test, was performed with the antenna removed from the GHz chassis. The limb and space ports viewed nominally identical cooled loads during a long period of switching between targets and ports. This test confirmed that baffle transmissions were as reported;

moreover, using small steps of the switching mirror, it also established how the purity of the space view degrades with switching mirror angle.

For the second test (the “Blue Sky” test), both space and antenna views of the complete GHz module were directed near zenith using large folding mirrors outside the door of the assembly facility [7, Figure 8]. For the antenna at each of 3 positions (the center and extrema of its scan range), switched observations were collected over a long period. This test established that the scan dependence of stray light, entering the FOV through spillover and internal reflections within the antenna, was small and had negligible spectral content.

F. Scan mechanism performance

Scan mechanism jitter was measured twice: once prior to delivery of the scan actuator for integration with the antenna, and again after assembly of the GHz module and delivery for spacecraft integration. Data from the latter measurement were sampled at 6 kHz and indicate a jitter of ~6 arcseconds peak-to-peak over time scales <0.17 s. This exceeds the requirement in Table I. The effect of jitter on the atmospheric retrievals is currently under investigation using in-orbit data. At the low frequency end, this jitter integrates down to give 1 arcsecond FOV boresight uncertainty for each 1/6 s MLS individual measurement, which meets the requirement for this time scale.

G. FOV Calibration Measurements

The FOV pattern was measured using a near-field range (NFR) constructed specifically for EOS MLS and assembled within the integration and test (I&T) facility at the Jet Propulsion Laboratory (JPL). References [13], [14], and [15] discuss NFR measurement theory, the NFR range built for MLS by Near-Field Systems (NSI) [16], and the details of the measurement RF techniques respectively. The near-field measurement technique was chosen for the FOV calibration for several reasons. With the GHz module antenna measuring 0.8 by 1.6 m, the far field for the highest frequency (660 GHz) begins at ~10 km. Atmospheric attenuation and the geography around JPL preclude measuring the beam patterns in the far field. By locating the NFR within the I&T facility, assembly, spectral calibration, and software checkout were interleaved, speeding instrument delivery.

1) *Near Field Antenna Measurement Concept:* Briefly, the concept is to launch a tone from the antenna of interest and measure the relative phase and amplitude of the received signal as functions of position on a defined surface completely enclosing the the antenna. Fields in the far zone can then be calculated by integrating the contributions from every measured point. In practical terms, for a high gain antenna with very low edge illumination such as the one used on MLS, virtually all of the radiation focused onto the receivers passes through a plane immediately in front of the antenna. Hence the far field pattern can be calculated by integrating the complex electric field distribution over the scan plane. In our application the signal direction is reversed with the tone launched from a source scanned in a plane in front of the antenna and received by the instrument's RFEs.

For a high-gain antenna, Kirchoff-Huyghens integration, over the volume bounded by the aperture plane and the far-field forward hemisphere, gives a component of the radiated field [13] as

$$F(K_x, K_y) = \iint f(x, y) e^{-i(K_x x + K_y y)} dx dy \quad (2)$$

where F is proportional to the complex far-zone field component having the same polarization as $f(x, y)$ when $K_x = K_y = 0$

$$K_x = (2\pi/\lambda) \sin \theta \cos \phi$$

$$K_y = (2\pi/\lambda) \sin \theta \sin \phi$$

$f(x, y)$ = complex aperture field component
 θ, ϕ are far-field spherical coordinates
 x, y are aperture position coordinates.

Equation (2) is an exact Fourier transform. The integration limits can be reduced from $\pm\infty$ to finite values within which $f(x, y) \neq 0$: in our case the aperture size, extended first to include scattering features of the secondary reflector and support structure, then projected to the scan plane at the 6° angle which bounds Ω_A . In evaluation of (2) using a discrete Fourier transform, the Nyquist theorem gives the spacing of samples required to reduce aliasing within Ω_A .

2) *Near Field Scanner*: The mechanical scanner assembly, control electronics, and data acquisition software were procured from Near Field Systems, Inc. (NSI) of Carson California [16].¹ Figure 4 is a drawing of the NSI model 905V-8x8 scanner [14] developed for MLS. The scanner consists of a vertical granite rail that supports a vertical bearing track on which the probe rotation stage travels. This assembly travels on two horizontal tracks supported by granite beams. The whole assembly is bolted to a $13 \times 13 \times 5$ foot concrete seismic pad that is embedded in the floor, and is mechanically isolated from outside vibration by several inches of felt. The rails are leveled and straightened through adjustable feet under the rails. The RMS variation of the scanned surface was measured to be less than $5 \mu\text{m}$. The horizontal, vertical, and angular position of the stage is controlled through an interface box by two computers that also run the user interface and the NSI data analysis software. A blower delivers room temperature air to cool the motors. Air conditioners maintain the room temperature variations to 1°C or less with temperature cycling on a 20 minute or longer time scale.

3) *Electronics Design*: We developed phase and amplitude detection systems (microwave interferometers) for each of the four frequencies of the GHz radiometers. In each case the downconverter was the actual flight RFE. Directional couplers (10 dB) were permanently added to the coaxial line between the receiver front end and the second IF. The coupled signals were then directed to a breakout panel between radiators on the outside of the GHz Module. Additionally, test points were

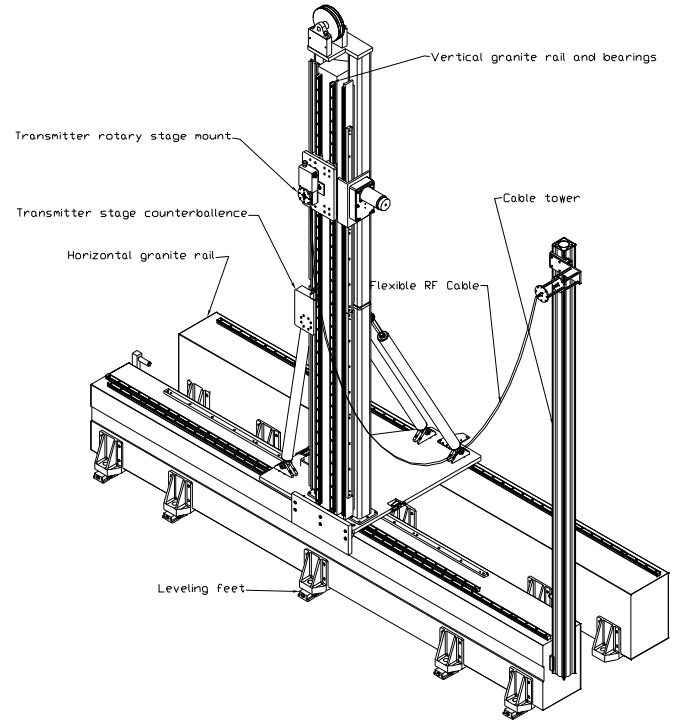


Fig. 4. NSI Model 905V-8x8 Near Field Scanner. The tower scans a total of eight feet horizontally. The probe mount on the tower scans eight feet vertically. Not shown are absorber panels on the tower and in front of the first horizontal granite support. Figure reproduced with permission of NSI.

included for measuring the frequency and phase for each of the RFE local oscillators (LOs).

The frequency and phase information for the source was carried on a 15 foot flexible coaxial cable running from a fixed position on the scanner to the moving probe mount. For each receiver band a temperature controlled test box was built to generate a frequency equal to the difference between the LO and the source. This was then compared to the IF signal from the RFE. The phase and amplitude were measured using an HP 8511 downconverter followed by an HP 8530 microwave receiver.

The cable performance was tested by transmitting an 18 GHz signal through the flexible cable to the translation stage and returning it to the receiver using an identical cable supported identically to the first. Over the portion of the scan plane used for these measurements, the phase delay of the 2 cables together varied by 1 degree. Fitting the variation to a planar tilt gives a pointing error of less than 3 arc seconds. The residual peak to peak variation is 0.3 degrees which is equivalent to an additional scan plane error of 7 microns peak to peak. Approximately half of this variation is due to cable hysteresis, *i.e.* measurements made as the probe scans up differed slightly from those scanning down. The use of rotary joints did not appear to improve this issue. All of the measurements presented used a cable rigidly supported to the probe and the cable support tower. A sheet metal support constrained the radius of curvature at the probe to one foot. The hysteresis is evident in the antenna measurements giving, for example, a 2 degree difference between adjacent scans at

¹NSI had previously constructed the NFR for the Submillimeter Wave Astronomy Satellite (SWAS) and the Microwave Instrument for the Rosetta Orbiter (MIRO): a 3x3 foot portable scanner using a flat granite slab as a reference and operated up to 560 GHz [17]. In addition to a higher frequency, our requirements included a larger 8x8 foot scan area.

240 GHz. The magnitude of this shift varied across the scan plane. In the data presented here, no attempt has been made to correct for any cable effects.

Figure 5 shows the signal path for the R2 interferometer. The R2 and R3 receivers use the same basic LO design, and multipliers to the submillimeter from the microwave frequencies were available for both receiver bands, so the interferometer design has only minor modifications for the different frequencies, band passes, and multiplication factors. The R2 and R3 receiver front ends use phase locked Gunn diode oscillators (GDOs) for their LO. The receiver front end downconverter mixers are sub-harmonically pumped meaning that the circuitry in the mixer effectively doubles the LO, so in the case of R2 a 95.95 GHz GDO drives a mixer such that $F_{IF} = |191.9 - F_{RF}|$. A portion of the GDO output is coupled to a detector for monitoring the GDO's output power and to a harmonic mixer that is used to phase lock the GDO to a harmonic of a dielectric resonant oscillator (DRO). The detector can be used as a harmonic mixer. To accommodate this application during FOV calibration, the coaxial line connecting the RFE to the receiver control unit is looped out and back in the same test port panel used for the IF test signals. A short loop of cable is removed during FOV calibration, allowing the detector to be used to sample the GDO signal.

The output from a synthesizer set at a frequency of F_S is fed into a power divider with half of its signal sent to the multiplier on the scanner stage where $F_{RF} = 12F_S$ is generated. The IF returned from the R2 RFE has a frequency $F_{IF} = |F_{RF} - 191.9 \text{ GHz}| = |12F_S - 191.9 \text{ GHz}|$ and carries the phase and amplitude information needed for the measurements. The second output from the power divider is used to pump the detector (being used as a harmonic mixer). The returned IF, $F_{Hmix} = |6F_S - 95.95 \text{ GHz}| = 0.5F_{IF}$, is separated from the pump signal in a diplexer then doubled to generate the reference signal for the microwave receiver. Only one transmitter at a time was mounted on the instrument and only one RF frequency was measured during each scan. A set of alignment pins ensured that the transmitter location was repeatable. Because the antenna is greatly under-illuminated and its gain is very high, the gain beyond ± 6 degrees from the boresight is very small. This allowed the use of feed horns with up to 25 dB gain to be used as probes for our system and allowed spacing between points of up to $\lambda/[2 \sin(6^\circ)]$.

4) *Near Field Scan Plane/Instrument Angle Measurement:* The GHz Module coordinate system is defined relative to an alignment cube mounted on the antenna bearing support structure near the antenna position encoder (APE). During spacecraft integration, the alignment of the GHz module relative to the THz Module and the spacecraft was measured optically using this cube. To place the measured antenna patterns in the angular coordinates of the GHz module, the angular position of the NFR scan plane was measured relative to this alignment cube. This required three of the four theodolites shown in Figure 6. The master theodolite (station 2) was located roughly in the scan plane approximately 12 feet to the right of the scanner. A reflective target was placed on the probe stage. The scanner was then commanded to move

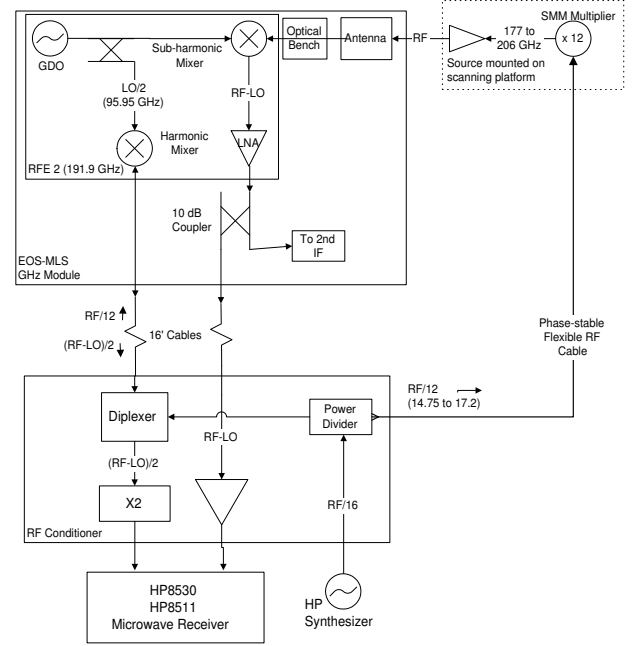


Fig. 5. Simplified block diagram for the interferometer for R2 beam pattern measurements. See text for description of operation.

the probe to 9 positions on the edges and center of the scan plane. The elevation and azimuth angles along with their x and y position in the scan plane were recorded for each point. A plane was fit to these measurements, thereby relating the scan plane to the coordinate system of the master theodolite. Two theodolites (stations 1 and 3) were positioned to autocollimate with perpendicular faces of the alignment cube and cross collimate with each other and the master station². Using the normal vectors to the cube faces and to the best-fit scan plane, we later transformed beam pointing angles to the coordinate system fixed to the alignment cube.

The angle of the antenna relative to the instrument was measured with the APE; hence the data set composed of FOV pattern pointing, theodolite angles, and APE readings constitutes the calibration of the APE, as described below. A fourth theodolite (station 4) was used to verify alignment of the antenna to the scan axis, by relating an alignment prism on the back of the secondary to the alignment cube. During calibration periods, theodolite measurements were conducted once in the evening at the start of a set of measurements, and again in the morning at the end of the measurement set.

5) *Testing Procedure:* Testing was conducted largely at night to limit the number of people in the test area during scanning, to limit their exposure to noise from the loud scanner motors, and to allow for spectral and sideband calibration along with final assembly efforts during regular work hours. The antenna actuator was not present during any of the FOV

²At each antenna position, a small translation of the master theodolite in the scan plane made the other stations visible, establishing a common azimuth and allowing a closure check of the measured angles.

tests, so the antenna angle relative to the instrument was set with a turnbuckle and recorded with the APE. After the antenna was set in position relative to the instrument, the instrument and its support stand were rotated so that the antenna was pointing nearly perpendicular to the scan plane. The support structure was then jacked up and lowered onto aluminum blocks placed on the seismic pad. The angle of the scan plane relative to the alignment cube was then measured. Before each set of patterns, a pattern at 234 GHz was quickly measured³ with large step sizes for a pointing reference. The 234 GHz system was then replaced by a transmitter and RF conditioner for the frequency to be measured. The system was allowed to stabilize thermally before measurements were made.

During the time to acquire a complete scan (up to 3 hours for R4) the phase and amplitude drifts in the interferometer were sampled periodically by interrupting the scan and returning the probe to a set of 4 positions in the highly illuminated center of the aperture. This technique, called Motion Tracking Interferometry (MTI) in the NSI literature (see [18] for patent information), gives two tilts and one phase offset for each set. These define both mechanical drift of the antenna relative to the scan plane and the drift in the differential phase delay through electronics. A typical interval between MTI points was 5 minutes. The time series of planar coefficients is used in post-processing to correct the aperture phase distribution to a reference established by the MTI point at the start or end of the scan. Amplitude drifts were generally less than 0.1 dB. Phase drifts were as much as 10 degrees for R1A and B, 8 degrees for R2 and R3, and 40 degrees for R4. The phases of the 4 positions generally drifted together, indicating that the changes were due to thermal drifts in the RF equipment. The maximum MTI measurements of the angular drift of the antenna boresight relative to a vector normal to the scan plane were on the order of 0.001°.

6) *Near field pattern results:* The 6 or 7 frequencies required to characterize the FOV in each band had generally been duplicated in the RFE pattern characterizations, allowing us to check the models for propagation from feed space to the antenna aperture. Figure 8 compares a measured aperture field to projections from RFE patterns. Both shape and size of the field amplitude agree within the primary aperture; the cross-polarized distribution is reduced by the polarizing grid as noted previously in Figure 3, with a maximum discrepancy of 5 dB at -40 dB due to model uncertainty in the alignment of grid and feed relative to the antenna.

Cross-polarized patterns were measured at scan angle and frequency spacings coarser than those measured for the co-polarized patterns. Although transmitter roll angles for co- and cross-polarized patterns were orthogonal to within the positioner accuracy of 0.1°, we were unable to measure the probe polarization with respect to scanner coordinates to better than 0.7°. Therefore, polarization angles reported to the flight software have the design values with $\pm 0.5^\circ$ tolerance due to

³The alignment of the field of view to the instrument is of secondary importance to the alignment of the receivers relative to each other. The 234 GHz line of $O^{18}O$ is MLS's best line for measuring pressure and temperature, so all pointing measurements were referenced to this line.

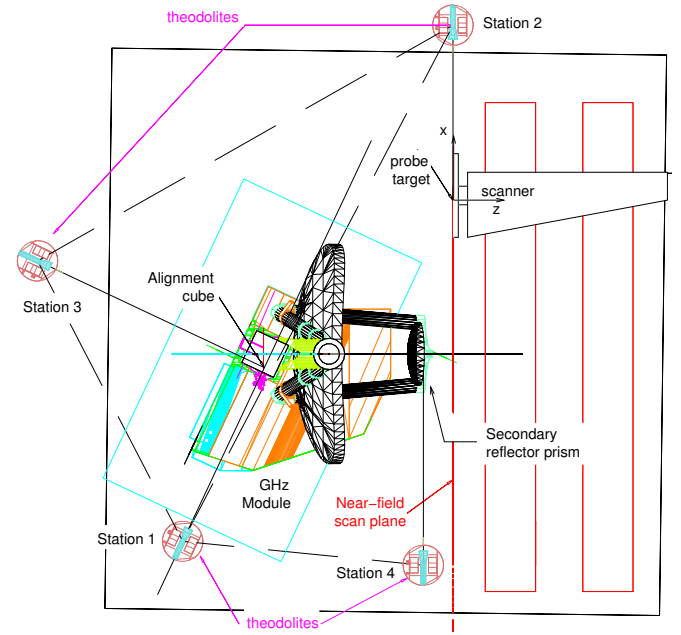


Fig. 6. Plan view of RF/optical alignment measurements in the Near Field Range.



Fig. 7. GHZ Module in the Near Field Range for definitive FOV calibration after environmental tests. The camera was near theodolite station 2 in Figure 6.

fabrication.

The frayed contours at the lowest co-polarized near field amplitudes in Figure 8 appear for all radiometers, but are less prominent for R1A, R1B, and R4. They lie outside the primary aperture in all cases except the $+x$ side of R4, due to feed pattern asymmetry discussed below. Their spatial scale is proportional to wavelength and larger than the sample size, so their effect is captured in the wide-angle regions of the far-field pattern. This structure changes only slightly with antenna scan angle, and since the phase in this region shows ripples concentric with the aperture edge, we believe this field results from edge diffraction at the rim of the primary reflector. For the elliptical aperture, the rim is not a planar curve, and the path length from the diffraction point to the scan plane, plus the varying phase illumination of the feed, give rise to interference. For R1A and R1B the tape used to terminate the reflector edge is less than $\lambda/10$ thick, which may explain the smoother contours. At the other extreme, the

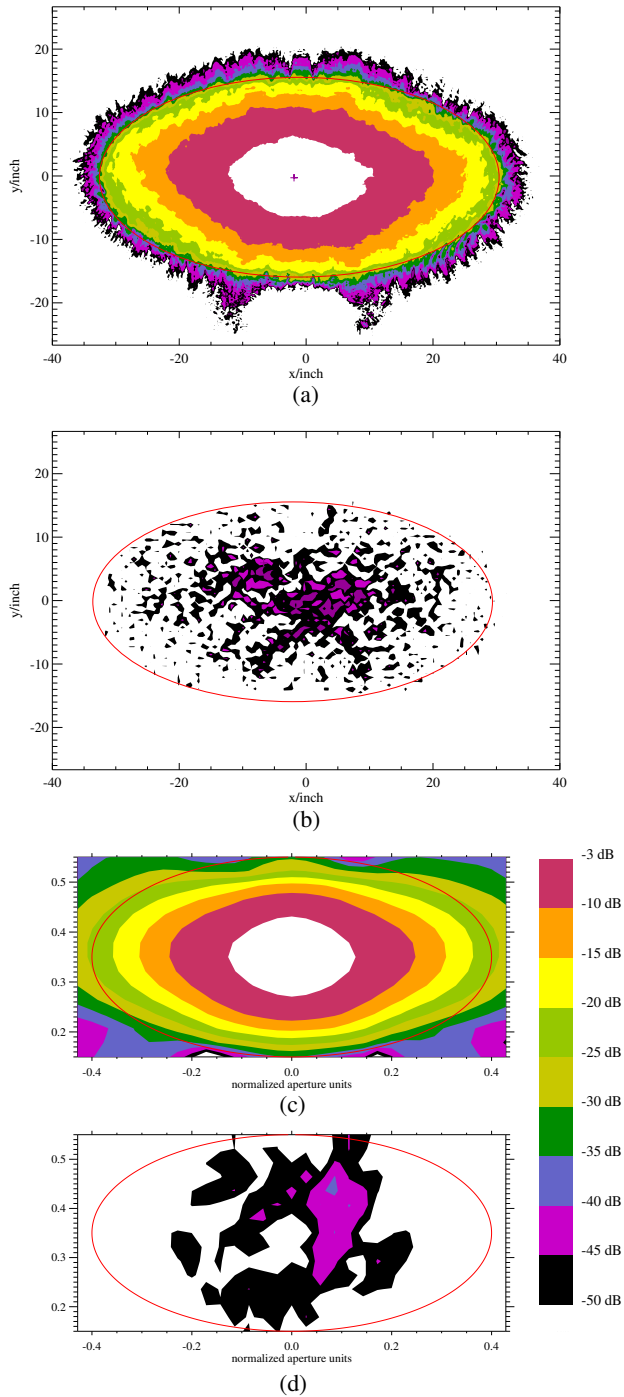


Fig. 8. 242.64 GHz Aperture Field: (a) Co-polarized and (b) cross-polarized amplitudes of the near field measurement compared to (c) co-polarized and (d) cross-polarized projections from RFE patterns. The red ellipses mark the 1.6 m \times 0.8 m aperture. Aperture coverage for the near-field patterns was $x = [-45, 45]$ inch, $y = [-38, 24]$ inch for both polarizations, sampled at (a) co-polarized $\Delta x = 0.212$ inch = 4.4λ , $\Delta y = 0.201$ inch = 4.1λ ; and (b) cross-polarized $\Delta x = 0.638$ inch = 13.2λ , $\Delta y = 0.602$ inch = 12.4λ . These ranges include internal antenna spillover through the secondary support arms and capture all appreciable power (from spillover and edge diffraction) which radiates into Ω_A .

lower edge illumination for R4 means that the diffraction falls below the -50 dB level shown. We used the measured intensity of projected feed patterns (instead of near-field patterns) to calculate edge diffraction losses. The portion radiated within Ω_A would be captured in the near field patterns and was thus excluded from η_r^{AD} in Table II. Therefore, edge diffraction is correctly represented in the total beam efficiency and its uncertainty (tabulated below), as well as in the stray light correction which Level 1 applies in calibrating limb radiances.

Figure 9 shows typical near- and far-field patterns obtained from the Near Field Range in 118 and 640 GHz bands. Cross-polarized patterns shown in the limb vertical cuts are from adjacent scans matched to the corresponding co-polarized patterns by assuming the transmitter power was unchanged when the probe was rotated 90°; from experience with RFE patterns this is valid for amplitude but not phase. Shadows of alignment tooling balls, on the peripheries of each reflector's clear aperture, can be discerned on the $x = 0$ plane of the amplitude and phase maps at 640 GHz. hysteresis, *i.e.* Many of the measurements exhibited a very low level contamination of the signal by the reference. This is evident from the faint ripples seen outside the primary aperture of the near field phase panels of Figure 9 after tilts within the aperture are removed. Since the corresponding amplitudes are very small, these have no effect on the far field patterns. The faint horizontal stripes within the aperture of the 640 GHz phase pattern are the result of MTI corrections.

Asymmetry in the near-field amplitude of R4 is a result of the toric feed mirror prescription: each feed mirror is elliptical in its own tangential (offset) plane and circular in the sagittal plane. This leads to distortions away from the principal planes, but the patterns remain symmetric about the offset plane. The configuration shown in Figure 2, and the orientation of multiplexer to antenna, make contours in the aperture egg-shaped for R1B, R2, and R4, but banana-shaped for R1A and R3. The asymmetry of R4 is more pronounced due to the higher edge taper of this radiometer (more of the distorted region illuminates the antenna).

We independently verified the near- to far- field transformation software which NSI supplied, by introducing measured near field patterns into the optics design software. This allowed us to apply the predicted effects of deformations due to gravity release and orbital thermal loads to the measured patterns. Since these effects were small, and confined to pointing changes, they have not been applied to the patterns for flight software use, but instead are bookkept separately for possible future enhancements of Level 1.

A persistent feature of the R3 far-field patterns was a region of grating lobes within 1° of boresight and 40 dB or more below the main lobe; Figure 10 shows an example. We believe these result from a superposition of images of dichroics $d2$ and $d3$, which both lie in the near field of the astigmatic beamwaist produced by the secondary reflector and matched by the feed mirror. We are currently studying the effect of these lobes on calculated forward model radiances.

R4 patterns had other unusual features that are seen in the far field panels of Figure 9: the diagonal strip through beam center and inclined 60° to horizontal appears in all R4 far-field

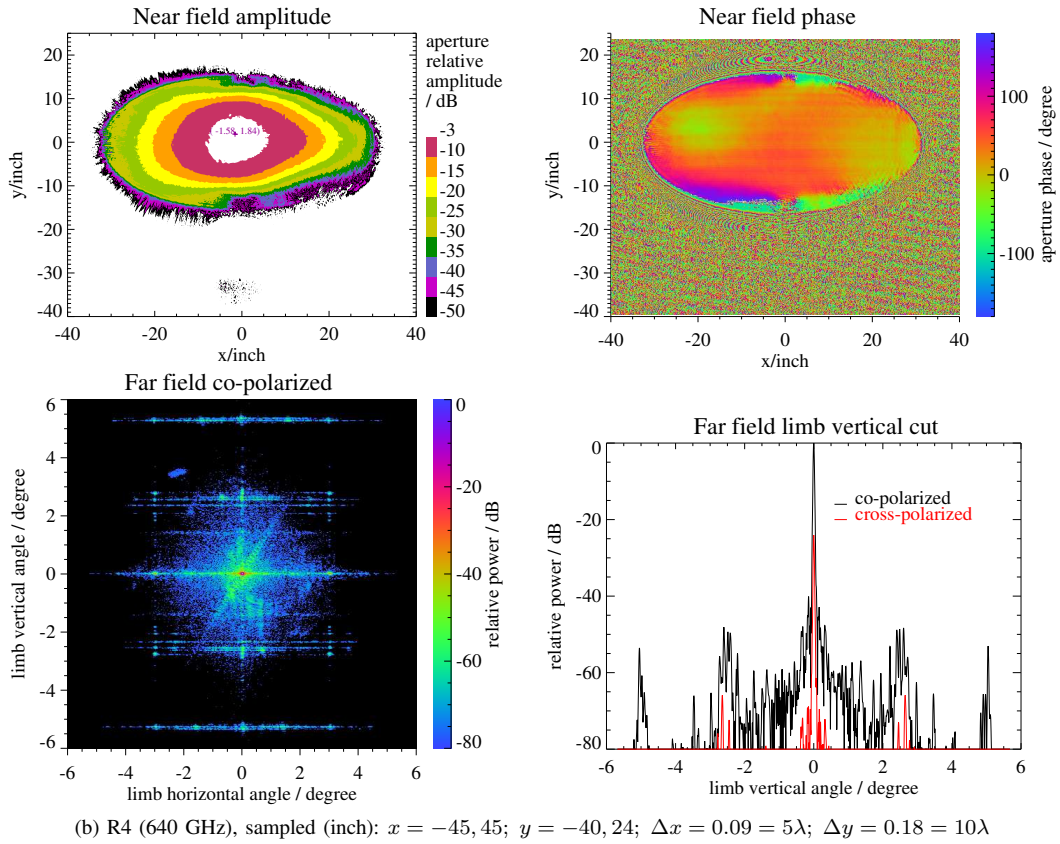
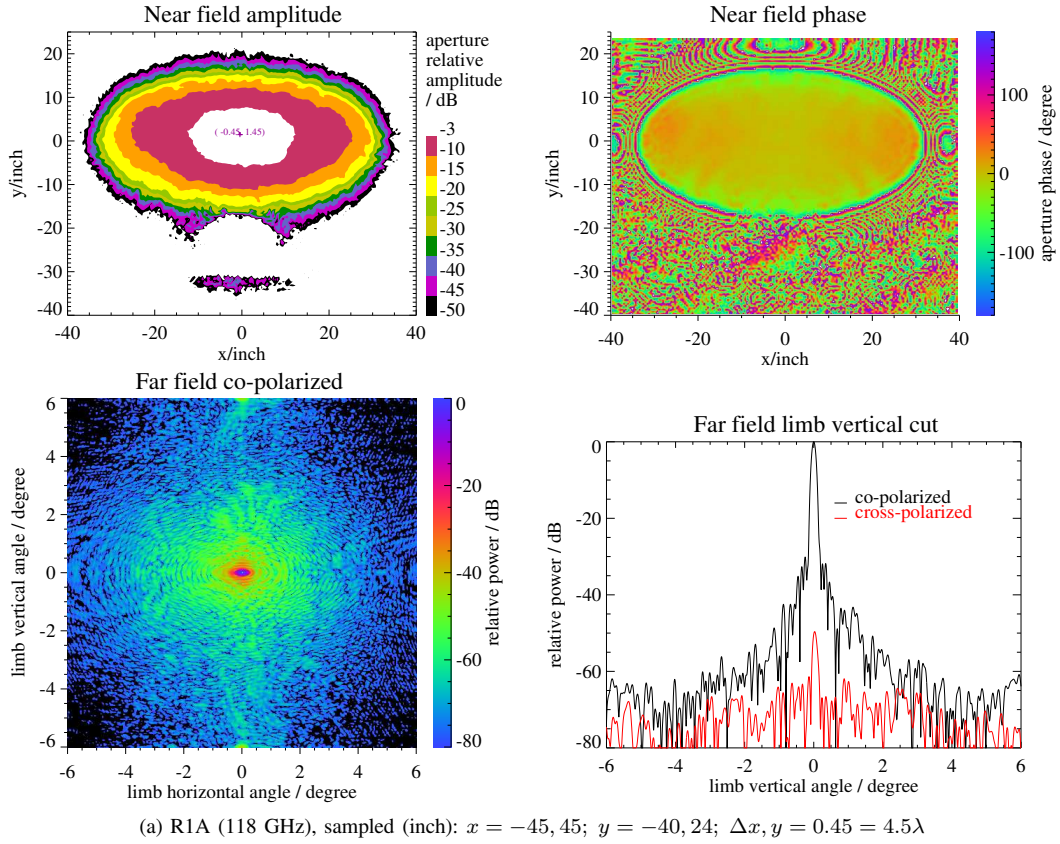


Fig. 9. Near and far field antenna pattern examples at 0 km nominal tangent height for (a) R1A and (b) R4 radiometers. The four panels shown for each radiometer are (clockwise from upper left): near field amplitude, near field phase, far field vertical cut (both polarizations), and far field amplitude map (rotated 90°). See text for discussion of faint stripes in the near field phase panels.

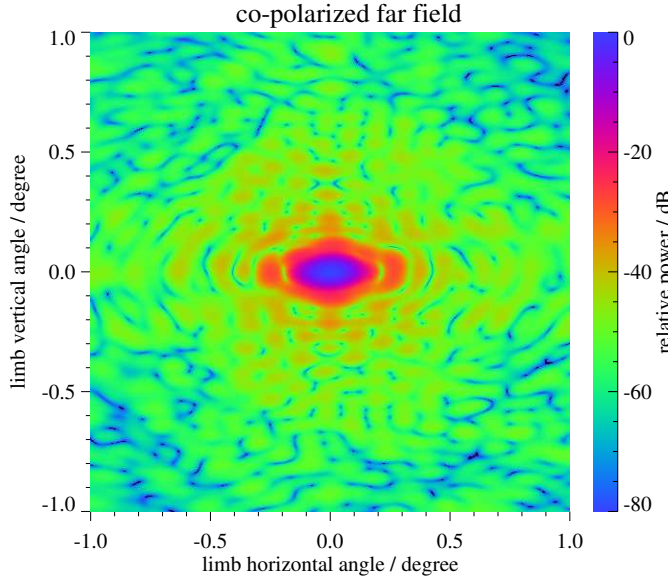


Fig. 10. Main lobe and nearby sidelobes of 242.64 GHz far-field pattern corresponding to Figure 8.

maps. Its source is unknown, but with a relative magnitude of -60 dB it has negligible effect on convolved radiances. The horizontal strips result from systematic phase errors (*e.g.*, cable hysteresis) that are repeated at several locations due to finite sample spacing. For pairs of scans taken at different spacings, they move in accordance with the sampling theorem.

Patterns in all radiometers were compared before and after the flight instrument environmental tests. In the case of R4, the RFE was also removed and re-installed between pattern sets. Nevertheless, patterns agreed to within 1 dB above -50 dB, and within 5 dB between -70 and -50 dB. The boresight co-alignment of R4 and R3 remained constant through tests within the measurement accuracy of $0.003^\circ(3\sigma)$.

We characterized the scan angle dependence of FOV by measuring near-field patterns at 4 scan angles: $\epsilon = 19.44^\circ$, 24.2° , 25.8° , and 30.54° (corresponding to tangent height $h_T \approx 300$ km, 83 km, 0 km, and -276 km, respectively). Test convolutions using these patterns gave scan angle dependences shown below (Table IV) to be very small for the normal atmospheric scan range (0–95 km) and degraded slightly for the total scan range.

Table III gives the beamwidth and beam efficiency ranges for all frequencies and scan angles measured after environmental tests. Efficiencies were calculated from the far-field patterns using post-processing software developed for analysis of the optics design, with a 2-dimensional numerical quadrature algorithm that had been validated for canonical cases (Airy patterns, tapered circular apertures, *etc.*). For each radiometer, the fractional difference between maximum and minimum values is roughly proportional to its fractional bandwidth. Maximum beamwidths and minimum beam efficiencies all meet the performance requirements in Table I.

Since the limb radiance variation is significant only in the vertical direction over much less than the $\pm 6^\circ$ domain treated in Level 2 processing, measured FOVs were *collapsed* into

TABLE III
MEASURED BEAMWIDTH AND BEAM EFFICIENCY RANGES OF THE GHZ FOVS, FOR ALL FREQUENCIES AND SCAN ANGLES MEASURED.

	HPBW [min,max] / $^\circ$		Beam Efficiency	
	Vertical	Horizontal	within Ω_A^a [min,max]	total ^b min
R1A	[0.107,0.118]	[0.227,0.245]	[0.978,0.984]	0.958
R1B	[0.111,0.119]	[0.220,0.236]	[0.980,0.984]	0.955
R2	[0.074,0.084]	[0.147,0.168]	[0.959,0.980]	0.953
R3	[0.058,0.064]	[0.116,0.126]	[0.962,0.973]	0.957
R4	[0.025,0.027]	[0.053,0.057]	[0.958,0.964]	0.947

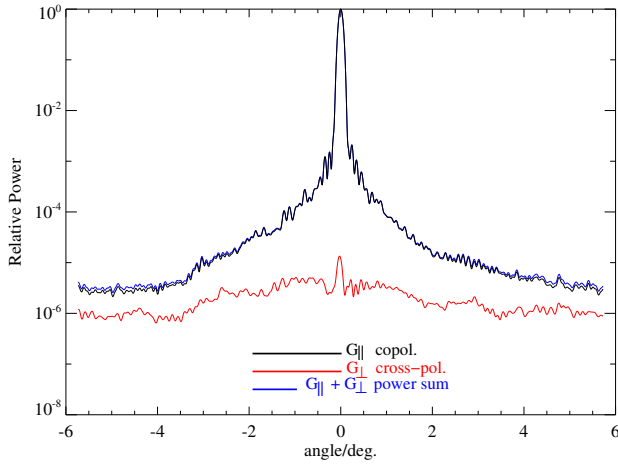
^aMeasured beam efficiencies repeated within 0.001 over 1 month intervals which included many transmitter swaps and motion of the GHZ antenna and its fixture.

^bTotal beam efficiency is the product of the beam efficiency within the measured region Ω_A with spillover and diffraction efficiencies $\eta_r^A \eta_{l,s}^1$ from Table II. The estimated uncertainty in total beam efficiency is ± 0.002 .

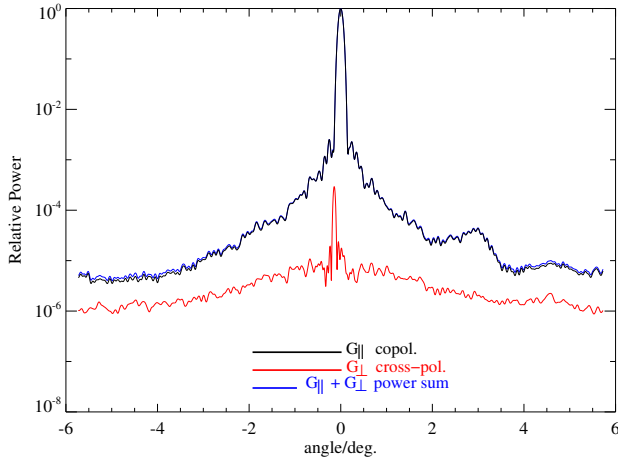
the vertical plane (*i.e.* integrated over the horizontal direction) as in [10], to provide 1-dimensional FOV functions for the Level 2 forward model. Cross-polarized patterns which had to be substituted from nearby frequencies or scan angles were shifted in level, using the corresponding co-polarized peaks. Co- and cross-polarized patterns were collapsed separately for digital autocorrelator channels at the center frequencies of R1A and R1B, but combined in quadrature before collapsing, for all other bands. Figure 11 shows the result for the patterns of Figure 9, plus R1B patterns for comparison with R1A. The higher cross-polarized power of R1B is consistent with its RFE patterns and results from a less symmetric horn and higher feed mirror edge taper. The bump at 3° appeared in several patterns of R1B, R2 and R3; we believe it is a range artifact, possibly reflection from a theodolite stand. Patterns with and without the bump were integrated with radiance kernels, showing a maximum error in convolved radiance of 0.01 K; therefore we have not removed the bump from forward model FOV data. On the other hand, the horizontal strips discussed earlier, at 2.5° and 4.9° from the center plane, had significant effect on convolved radiances and were removed from the collapsed patterns; interpolation across the gaps resulted in the four smooth patches in the R4 plot. These strips had negligible effect on beam efficiency.

We convolved collapsed patterns with the radiance kernels and evaluated radiance errors for the range of scan angles and frequencies measured, to show compliance with the FOV calibration requirement.

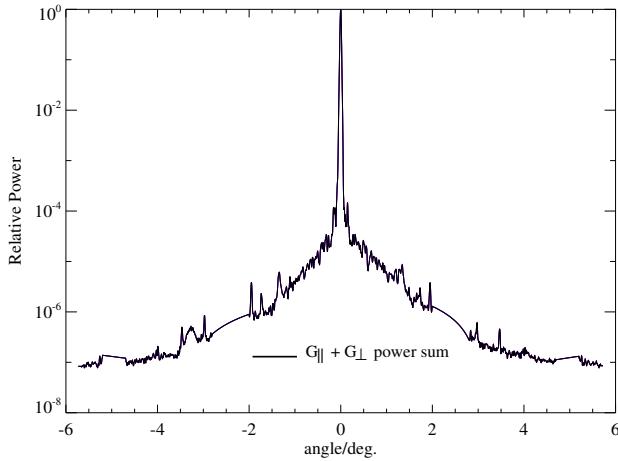
Boresight direction of the FOV (dFOV) was determined by a theodolite survey of the alignment cube and the scanner immediately before or after a pattern measurement in the 234 GHz pointing reference, as described earlier. This *fiducial* pattern was abbreviated to concentrate on main beam pointing rather than sidelobes. Interspersing fiducial patterns between those of other radiometers allowed the dFOV coincidence between radiometer FOVs to be evaluated quickly and without inflation of uncertainties which would result from going through an optical alignment data path. This method verified the co-alignment through environmental test, mentioned above.



(a)



(b)



(c)

Fig. 11. Definitive FOV functions for Level 2 Processing Coefficients: (a) R1A and (b) R1B in both polarizations, and (c) R4 Band 14 unpolarized.

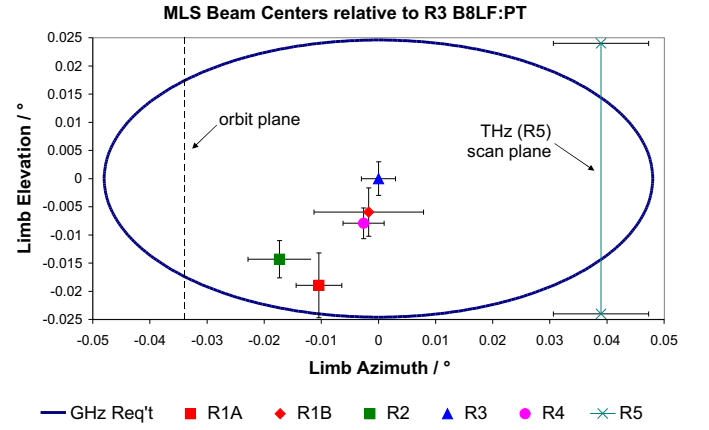


Fig. 12. Bore-sight coincidence of EOS MLS FOVs. Error bars include 3σ measurement uncertainty, variation with IF, and residual from the scan model fit of data taken at 4 scan angles. This view shows bore-sights projected onto a plane centered on the R3 limb tangent point, as seen from the MLS.

During the definitive FOV calibration after environmental tests, dFOV was measured, along with the scan encoder reading, at the 4 scan angles listed above, to produce the the encoder/dFOV/cube calibration data. In later analysis, a time series of fiducial pointing information was constructed, to permit interpolation of reference pointing angles and scan encoder readings onto the patterns of the other radiometers. A regression model was developed to fit heuristic misalignment parameters to dFOVs measured for each GHz radiometer, along with dFOV coincidence measured using fiducial patterns only. The results are combined with data, obtained during spacecraft integration, which give the bore-sight coincidence of GHz and THz pointing channels and their directions in spacecraft reference coordinates. Values for each band were provided to the flight software, and are plotted in Figure 12 as binned by radiometer.

The grouping of bore-sight directions in Figure 12 results from the tolerances on elements of the GHz optical multiplexer. Without detailed information on the as-built alignment of beam splitter mounting surfaces, we could not correlate the bore-sights of the different radiometers quantitatively. However, within a given radiometer it was possible to correlate the frequency dependence of feed phase centers and bore-sight angles with aperture fields from the Near Field Range. The scatter was less than measurement uncertainty and repeatability (typically 0.05λ for lateral phase center position and 0.02° for bore-sight angle in the feed patterns) for all radiometers except the 118 GHz R1A and R1B (E-planes only). Near field measurements of R1B showed horizontal pointing anomalies as large as 0.007° (far-field) at two frequencies where both horn and RFE patterns had shown unusual bore-sight pointing. Antenna patterns of R1A showed a smaller frequency-dependent vertical pointing excursion of 0.004° , which matches the 0.2λ variation of RFE lateral phase center position in both shape and magnitude. Each of the R1A deviations is about 4 times the repeatability for the respective test range, given that both transmitter and test article remained fixed for the frequency measurements.

IV. IN-ORBIT PERFORMANCE

All FOV-related engineering data observed during the in-orbit activation of EOS MLS were within pre-launch predictions. Primary reflector temperatures matched predictions within 5° over the full $[-10, +75]^\circ$ C range (Aura's mid-summer launch date put the angle β between sun and orbit plane near its minimum), as did the secondary and tertiary temperatures. With the scan stopped, a small relative rotation of the antenna, due to differing thermal expansion coefficients within the scan actuator and antenna under varying orbital heat loads, matched model predictions within 10–20 arcseconds.

For the following discussion of operation of the MLS, the repeat period of a scan through Earth's limb, nominally 24.7 s, is called a *major frame* (MAF). The 240 MAFs per orbit each nominally consist of 148 *minor frames* (MIFs), whose length is the instrument integration time, approximately 1/6 s.

A. Stray Radiances

Several tests performed in activation helped confirm the low stray light levels predicted before launch. These include: periods of large amplitude scanning, a pitch-up maneuver (20° for 1/3 orbit and 5° for 3 orbits) to scan far sidelobes of the FOV over Earth's limb, and a slow sweep of the switching mirror through 360° with the antenna at a fixed scan angle. Among other things, this sweep checks for stray reflections within the switching mirror cavity and quantifies mirror angle sensitivity, for comparison with dual-cold load tests. Results of all these tests are still under study, but all show that stray-light FOV parameters in Table II have error bars at least as small as reported before launch, and we expect future calibration refinements to reduce these uncertainties.

1) *Ohmic loss (reflectivity) corrections*: Level 1 uses the reflectivities in Table II and reflector temperatures, measured once per MAF at 17 points on the GHz antenna, to correct for reflector emission as part of radiance calibration [7]. Time series of calibrated radiances for high-altitude ($h_T > 87$ km) MIFs showed both offsets and ripple having a period and shape similar to the average primary reflector temperature. This suggested that reflectivities in flight differ from those measured before launch, by statistically significant amounts for R3 (slightly lower than before launch) and R4 (higher).

We retrieved new values of reflectivity using high-altitude MIFs from 28 July and 1 September 2004. For the new values we have assumed that, due to fabrication differences mentioned earlier, the reflectivities of the secondary and tertiary reflectors differ from that of the primary. This removed a previous Fresnel constraint between the primary and the other reflectors; instead we made the average calibrated high-altitude radiance match the (frequency-dependent) Planck value. Revised values, shown in Table II, were incorporated in version 1.5 of the MLS data processing software (the version producing the first publicly released data).

Figure 13 is a time series of radiances in selected bands of R1A and R2 averaged over high-altitude MIFs on 20 December 2004 (R3 and R4 are omitted for clarity; this day was chosen to illustrate both radiance offset and contamination by the moon in the space view, discussed below). Its left

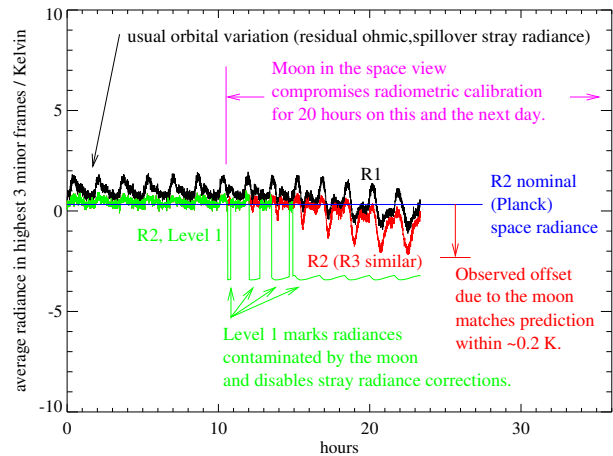


Fig. 13. Time series of high-altitude radiances on 2004 December 20, showing residual orbital variation after corrections for ohmic losses, and at right the moon entering the GHz space view about midday. The black and red curves are R1A and R2 radiance, respectively. Steps in the green curve indicate R2 radiance flagged by Level 1 for moon contamination. The blue line is the nominal R2 Planck space radiance. R3 and R4 radiances, not shown, have similar shapes but with higher noise.

half shows results after reflectivity adjustments. Although all these time series now have the correct mean values, they still show residual orbital variations. These have negligible spectral variation within radiometer bands, but are greatest for R1, whose baffle and spillover losses are largest due to reduced edge taper. This implies that the the Level 1 correction for stray radiance (using the transmissions in Table II) still needs to be refined. The last steps of Level 1 calculate empirical baseline corrections [7], whose purpose is to protect the geophysical retrievals from residual instrumental artifacts, such as these radiance offsets. However, in order to correct our physical model of radiometric calibration, we are continuing to review the stray radiances and to resolve the remaining orbital ripple into ohmic and spillover components. We are also devising laboratory measurements, using an engineering model of the R4 receiver, to understand the dependence of ohmic loss on incidence angle, polarization and reflector construction.

2) *Moon contamination of space view radiances*: Since the GHz space view points anti-parallel to Aura's orbit normal vector, the moon appears in the space view for ~ 20 hours twice a year, adding a radiance up to 4 K which compromises the Level 1 radiometric calibration. The right half of Figure 13 shows how incorrect low values of limb radiance result as the moon approaches the boresight of the space beam. The same plot for the next day is roughly reversed, as the moon spirals out of the beam. A moon radiance model described below predicts the radiance contamination within about 0.2 K, so we are customizing local versions of the Level 1 software in order to reclaim the data lost during these events.

B. Moon calibration of pointing offsets

The moon also appears periodically in the limb view of MLS, offering opportunities for in-orbit FOV calibration. Retrieved profiles of atmospheric constituents depend on knowl-

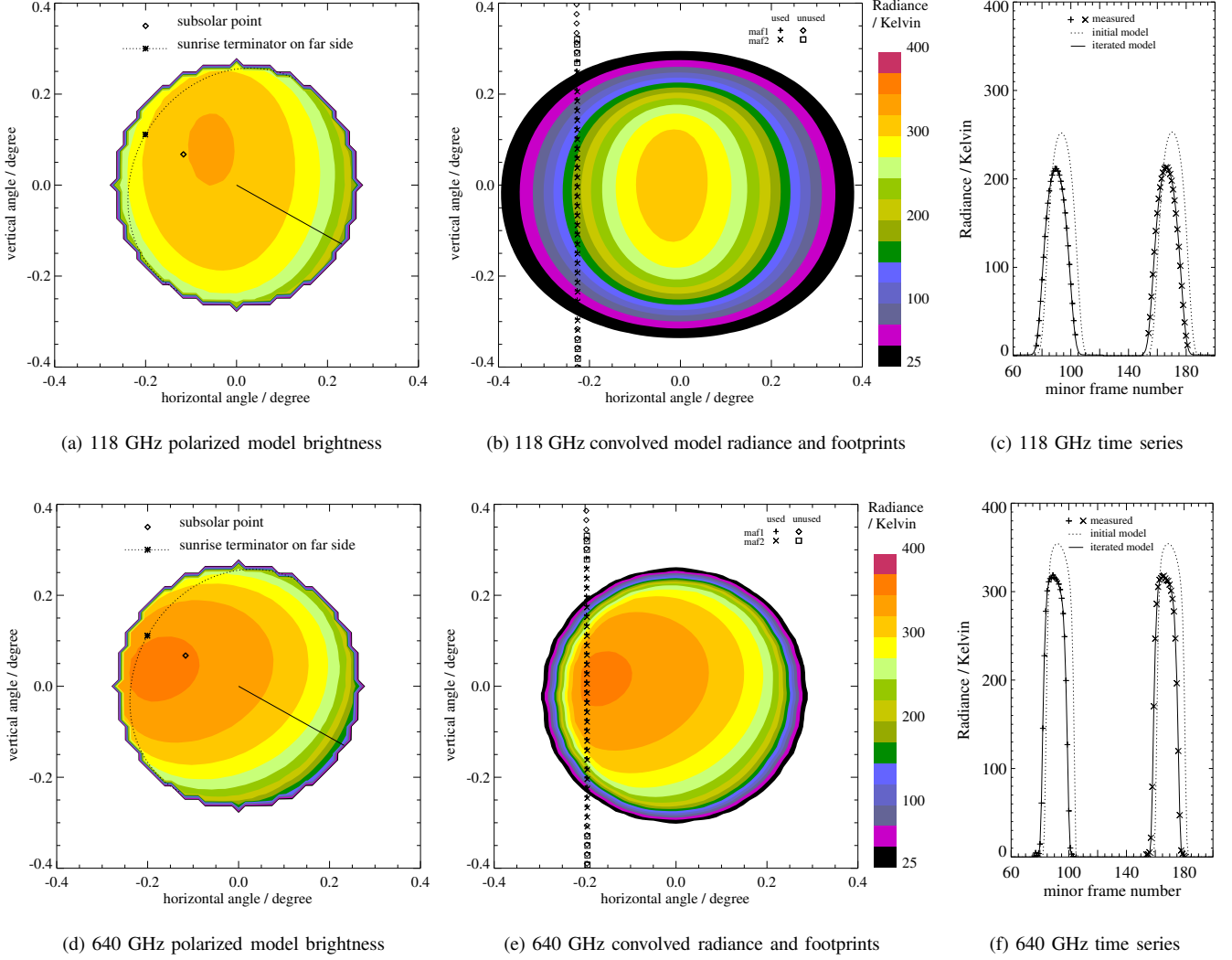


Fig. 14. Example of FOV scan through the moon on 20 September 2005, for 118 GHz (a–c) and 640 GHz (d–f). Panels (a,d) are model radiances incident on the MLS antenna, showing polarization dependence and model angular resolution. (b,e) show model radiances after convolution with the FOV patterns, overlaid with scan footprints. (c,f) show both measured (symbols) and model radiance time series before (dashed) and after (solid) iterative solution for pointing and scale factor A_M .

edge of radiometer FOV pointing offsets (dFOV) relative to the 234 GHz pointing reference [19]. During early months of the UARS mission, discrepancies between retrieved ozone profiles from two UARS MLS radiometers were attributed to errors in pre-launch values of relative pointing. This led us to use the moon as a pointing calibration source to establish offsets between in-flight radiometer FOVs [10]. For EOS MLS, the 0.003° measurement uncertainty we found for pre-launch dFOV corresponds to a 1% error in profile magnitude, somewhat less than the differences found in current MLS retrievals and intercomparisons [19]. To confirm our pre-launch values of dFOV coincidence and to reduce their uncertainties, we have begun a series of moon scans for EOS MLS, similar to those done for UARS MLS.

The moon crosses Aura’s orbit plane twice per month, with lunar phases within a few degrees of -155° (near new moon) and $+25^\circ$ (near full moon). Given the periods of the moon and Aura, the scan ranges of THz and GHZ FOVs cross the

lunar disk on about 60% of these opportunities. As of this writing, we have replaced the nominal atmospheric scan with a special scan, well above the atmosphere, for seven of these events. The scan moves the THz and GHZ FOVs in opposing “sawtooth” scans; their ranges are chosen to guarantee that each will have at least one string of 30 or more limb MIFs viewing the moon, and two if the moon does not appear in calibration views.

Algorithms for retrieving pointing offsets from moon radiances were developed for UARS MLS [10]. Measured radiances are compared to predictions (from an Apollo-based lunar microwave model [20]) that are convolved with the 2-dimensional measured FOVs, smeared slightly by the ~ 0.167 s integration time. We can relate measured radiances to the model map and its gradient by two pointing angles and a scaling factor A_M . These 3 parameters are estimated by minimizing the sum of squared radiance residuals for the ~ 60 MIFs in each moon crossing. Unlike UARS MLS, the EOS

TABLE IV
SUMMARY OF FOV UNCERTAINTIES

	R1A	R1B	R2	R3	R4
Level 1 scaling uncertainty (3σ)	0.17%	0.23%	0.20%	0.21%	0.38%
HPBW uncertainty (3σ)	0.004°	0.006°	0.002°	0.001°	0.0015°
Pointing offset uncertainty (all GHz and THz relative to reference)					
Pre-launch + crude moon model			$\pm 0.003^\circ$		
expected from re-fined moon model			$3\sigma = 0.0006^\circ$		
Error in convolved radiance due to scan dependence of FOV / K					
$h_T \in [0, 83]$ km	± 0.15	± 0.12	± 0.09	± 0.16	± 0.24
$\in [-280, 300]$ km	± 0.4	± 0.3	± 0.4	± 1.2	± 0.27

MLS FOVs move across the moon only in the limb vertical direction, so the retrieval has difficulty distinguishing A_M from limb horizontal misalignment;⁴ hence in the final retrieval we constrain A_M to be a constant determined from all scans.

A typical result is in Figure 14, showing moon model radiance maps before and after convolution with the FOVs of two MLS radiometers. These data are still being analyzed, but preliminary results confirm the pre-launch measurements of boresight coincidence, shown in Figure 12, to the accuracy of the near field measurements, $\pm 0.003^\circ$ (± 150 m). Moreover, the THz FOV appears to point 0.007° (350 m, with the same uncertainty) higher in the atmosphere than the GHz FOV, after encoder angles are corrected for all misalignments known before launch. With recent extension of the MLS and lunar brightness models from 63–205 GHz up to 2.5 THz, we expect to refine pointing knowledge to a level of $3\sigma = 0.0006^\circ$.

V. CONCLUSIONS

This paper has described the GHz optics design and calibration. Ground calibration provided all FOV parameters and functions required for flight data processing. In-flight evaluation of these is still in progress, but so far has validated all these except ohmic loss, some of whose values we have revised using in-flight data and provided for the current version of data processing software. We are developing a laboratory measurement program to corroborate these changes.

Table IV summarizes systematic uncertainties in FOV. Scaling uncertainties have been separated from radiance offsets, which are removed by Level 2 processing. The principal contributions to scaling uncertainty are ohmic loss uncertainty and the variation (with IF) of the difference between limb and space beam solid angles from the feed patterns. The table also contains estimates of uncertainties in the detailed FOV patterns. Since the small frequency dependences within each radiometer have been captured by providing band-dependent patterns to the flight software, the remaining uncertainty is dominated by residual scan angle dependences, themselves also small as shown.

⁴Singularity of this retrieval, expressed by its matrix condition number, is typically $5\times$ greater for EOS MLS than for the UARS MLS moon scans.

The GHz optics and FOV calibration have met all requirements except for jitter in the scan mechanism, which is now under study using in-orbit data. We continue to maintain and refine calibrations through the duration of the mission.

ACKNOWLEDGMENT

The authors wish to acknowledge the work of many members of the MLS science and instrument teams whose contributions made the design and FOV calibration of the GHz optics possible. We would especially like to thank Janet Squires for developing the NASTRAN deformations model; Nasrat Raouf for help with the optics model and feed mirror procurement; Eugene Poyorena, Mark Thompson, and Nick DeLuca for theodolite and opto-mechanical measurements in all assembly phases; Jack Hardy, Robert Dengler and Ray Swindlehurst for support of receiver patterns, and for help in the conception and implementation of the Near Field Range, as well as Dan Slater and Greg Hindman of NSI; and other colleagues too numerous to mention here. We also particularly thank Stephen Keihm for enhancing the moon radiance models from UARS MLS frequencies up to 2.5 THz.

REFERENCES

- [1] J. W. Waters *et al.*, "The Earth Observing System Microwave Limb Sounder (EOS MLS)," *IEEE Transactions on Geoscience and Remote Sensing*, vol. This issue.
- [2] —, "The Upper Atmosphere Research Satellite and Earth Observing System Microwave Limb Sounder Experiments," *Journal of the Atmospheric Sciences*, vol. 56, pp. 194–218, January 1999.
- [3] F. T. Ulaby, R. K. Moore, and A. K. Fung, *Microwave Remote Sensing, Active and Passive*. Addison-Wesley, 1981.
- [4] H. M. Pickett, "Microwave Limb Sounder THz Module on Aura," *IEEE Transactions on Geoscience and Remote Sensing*, vol. This issue.
- [5] J. W. Waters and R. F. Jarnot, "Science Requirements on the EOS MLS Instrument and Data Processing," JPL D-14421, Rev. 3, 26 February 2002, available on request.
- [6] W. G. Read *et al.*, "The Clear-Sky Unpolarized Forward Model for the EOS Aura Microwave Limb Sounder," *IEEE Transactions on Geoscience and Remote Sensing*, vol. This issue.
- [7] R. F. Jarnot, V. S. Perun, and M. J. Schwartz, "Radiometric and Spectral Performance and Calibration of the GHz Bands of EOS MLS," *IEEE Transactions on Geoscience and Remote Sensing*, vol. This issue.
- [8] F. T. Barath *et al.*, "The Upper Atmosphere Research Satellite Microwave Limb Sounder Instrument," *Journal of Geophysical Research*, vol. 98, no. D6, pp. 10,751–10,762, June 1993.
- [9] J. Ruze, "Antenna tolerance theory—a review," *Proceedings of the IEEE*, vol. 54, no. 4, pp. 633–640, April 1966.
- [10] R. F. Jarnot *et al.*, "Calibration of the Microwave Limb Sounder on the Upper Atmosphere Research Satellite," *Journal of Geophysical Research*, vol. 101, no. 6, pp. 9957–9982, April 1996.
- [11] P. Siegel, R. Dengler, and J. Chen, "THz dichroic plates for use at high angles of incidence," *IEEE Microwave and Guided Wave Letters*, vol. 1, no. 1, January 1991.
- [12] R. F. Jarnot, R. E. Cofield, H. M. Pickett, and P. C. Stek, "EOS MLS Instrument Calibration Report," JPL D-26280, available by request from jarnot@mls.jpl.nasa.gov.
- [13] D. Slater, *Near Field Antenna Measurements*. Artech House, Inc., 1991, ISBN 0-89006-361-3.
- [14] D. Slater *et al.*, "A large aperture 650 GHz near-field measurement system for the Earth Observing System Microwave Limb Sounder," in *Antenna Measurement Techniques Association Conference 20th ESTEC Antenna Workshop on Millimetre Wave Antenna*, Oct. 2001.
- [15] P. Stek and R. Cofield, "Near-field measurements of a high gain 110 to 660 GHz antenna for remote earth sensing," in preparation.
- [16] G. Hindman *et al.* (2004) Nearfield Systems homepage. Nearfield Systems, Inc. [Online]. Available: <http://www.nearfield.com>

- [17] N. Erickson and V. Tolls, "Near-Field Measurements of the SWAS Antenna," in *20th ESTEC Antenna Workshop on Millimetre Wave Antenna Technology and Antenna Measurements*, Noordwijk, The Netherlands, June 18–20, 1997.
- [18] D. Slater. (1995, May) Three-axis motion tracking interferometer for measurement and correction of positional errors between an article under test and a measurement probe. United States Patent 5419631. [Online]. Available: <http://www.nearfield.com/Patents/tmt.htm>
- [19] L. Froidevaux *et al.*, "Early Validation Analyses of Atmospheric Profiles from EOS MLS on the Aura Satellite," *IEEE Transactions on Geoscience and Remote Sensing*, vol. This issue.
- [20] S. Keihm, "Interpretation of the lunar microwave brightness temperature spectrum: Feasibility of orbital heat flow mapping," *Icarus*, vol. 60, pp. 568–589, 1984.



Richard E. Cofield (M'83) received the B.S. degree in Applied Physics from the California Institute of Technology in 1974, and the M.S. degree in Electrical Engineering from the University of Southern California in 1982. In 1978 he joined the Jet Propulsion Laboratory, Pasadena, California, to design, analyze and calibrate antenna and optical systems for spaceborne radar and radiometer instruments observing the Earth. His interests include reflector antennas and quasi-optical feed systems.



Paul C. Stek (Ph.D.'97) received the B.S. degree in Engineering Physics from the University of California at Berkeley in 1986, and the Ph.D. degree in Physics from the Massachusetts Institute of Technology in 1997. In 1997 he joined the Jet Propulsion Laboratory, Pasadena, California, to develop millimeter and sub-millimeter wave technology for remote sensing. His interests include radiometer development and calibration.